Typhoon statistics in variable resolution Asia-Pacific CAM-SE

Duofan Zheng[1], Shao-Yi Lee[2], Wenting Lin[3], Qi Ran[1], Wenjie Dong[1]

[1]School of Atmospheric Sciences Sun Yat-Sen University, Key Laboratory of Tropical Atmosphere-Ocean System Ministry of Education, and Southern Marine Science and Engineering Guangdong Laboratory, Zhuhai 519082, China.

5   [2]Disaster Prevention Research Institute, Kyoto University, Uji, 611-0011, Japan

[3]Zhuhai Meteorological Bureau, Zhuhai 519082, China

Correspondence to: Wenjie Dong (dongwj3@mail.sysu.edu.cn)

Abstract. Three Asia-centric configurations of the Community Atmosphere Model with the Spectral Element dynamical core (CAM-SE) were set up, with horizontal resolutions of approximately 1° globally, 1° increasing to 0.5° over the Asia-Pacific,

10   and 1° increasing to 0.25°. A typhoon tracking algorithm was developed to extract the tracks of typhoons generated by the simulations. The typhoon intensities were bias corrected using scale conversion factors calculated from a comparison of tracks extracted from the European Centre for Medium-Range Weather Forecasts Reanalysis version 5 (ERA5) and the International Best Track Archive for Climate Stewardship (IBTrACS). Typhoon frequency, track density, genesis locations, and energy were calculated from 20 years of equilibrium climate simulations using the three configurations, then compared with the

15   statistics from ERA5 and IBTrACS. The 1° and 0.5° CAM-SE simulations were unable to produce enough "Super Typhoons" (maximum sustained central wind speed $\geqslant$ 51 m s^{-1}) even after bias correction. The 0.25° simulation managed to produce enough "Super Typhoons", indicating that at least 0.25° horizontal resolution is advisable for global climate simulations to produce appropriate "Super Typhoon" statistics. The regionally refined 0.25° CAM-SE configuration was estimated to be at least two times faster than a globally 0.25° typical configuration.

1 Introduction

In 2017 and 2018, the Pearl River Delta in southern China was successively struck by Typhoons Hato and Mangkhut, respectively. Hato rapidly intensified to Super Typhoon intensity just before landfall, while Mangkhut was consistently of Super Typhoon intensity from the Pacific but began to weaken after its first landfall at Luzon, Philippines (Choy et al., 2022). The two typhoons caused extensive destruction in the highly populated Pearl River Delta region. In the case of Mangkhut, the potential damage was fortunately ameliorated by the human factor of preparedness from recent experience (Li et al., 2022), as well as the natural factor of attenuation by a first landfall over mountainous Luzon instead of just passing through the Straits of Luzon. In 2023, the region was struck by Typhoon Saola, another Super Typhoon which this time passed through the Straits of Luzon and remained at Super Typhoon intensity until landfall (Chan et al., 2024).

It is concerning that the region only experienced 4 Super Typhoons in the 71-year period of 1946–2016, but have already experienced 3 Super Typhoons in the 7-year period of 2017-2023 (according to the Hong Kong Observatory at https://www.hko.gov.hk/en/informtc/historical_tc/metinfo_wind.htm). A Pseudo-Global Warming experiment carried out on Mangkhut indicated a similar typhoon in conditions of 2 °C warmer sea surface temperatures would be ten percent stronger (Wang et al., 2024). It is hence plausible that climate change played a role in the recent increased number of Super Typhoons reaching the region. The impact of warmer climates in intensifying such typhoons is well-studied, but the authors would like to examine the impact on the climate statistics of typhoon generation and tracks, which typically necessitates multi-decadal simulations on climate models. Before such a study, it is necessary to ascertain that the climate model can produce acceptable statistics of Super Typhoons.

It is known that sufficiently high horizontal resolution is required for the accurate simulation of typhoons. For example, a sensitivity study carried out by Murakami and Sugi (2010) using general circulation model simulations with horizontal resolutions ranging from about 180 km to 20 km showed that the 20 km simulation was the best at simulating "extremely intense" tropical cyclones (maximum wind velocity $\geqslant$ 60 m s^{-1}). The extremely intense tropical cyclones were still underestimated at 20 km resolution, but practically typhoons do not need to be perfectly reproduced as long as the appropriate statistics can be retrieved after bias correction. Unfortunately, the computational cost involved in performing 20 km multi-decadal global simulations is prohibitive for most researchers. Fortunately, it may not be necessary to run the simulations at high resolution everywhere, by using variable resolution global circulation models.

The Spectral Element (SE) method was originally proposed in the field of fluid mechanics (Patera et al., 1984). It was later formulated for the shallow water equation on the sphere (Taylor et al., 1997), and progressively developed and tested for increasing complex cases (see Dennis et al., 2012 for a summary). Under SE discretization, the computational domain is broken up into rectangular regions, or elements. The surface of the globe is divided into quasi-uniform mesh spacings using the gnomic projection of a cubed-sphere grid (Sadourny et al.,1972). The spectral element model was realised as the the High-Order Method Modeling Environment (HOMME; Dennis et al., 2005), then later incorporated into the Community Atmosphere Model version 5 (CAM5; Neale et al., 2010) component of the Community Earth System Model (CESM) version 1 (Hurrell et al., 2013) as the as the SE dynamical core (CAM-SE; Dennis et al., 2012). An improved version was later released in in CESM version 2 (Lauritzen et al., 2018). Variable resolution CESM has been successfully used to study the impact of irrigation on California's climate (Huang et al., 2016), regional climate (Wu et al., 2017) and snowpack trends in the Rocky Mountains (Rhoades et al., 2018), and land-atmosphere coupling (Devanand et al., 2020). In particular, CAM-SE has been shown to be well-suited for tropical cyclone simulations over the Atlantic basin (Zarycki, 2014; Zarzycki and Jablonowski, 2014; Zarzycki and Jablonowski, 2015). Given the success over the Atlantic basin, the authors decided to experiment with similar configurations over the western Pacific.

The manuscript is structured as follows: Section 2 describes the model configuration, typhoon tracking algorithm, and verification method. Section 3 compares the typhoon statistics from the different model configurations with observation. Section 4 gives the conclusions.

2 Data and Method

2.1 Model description

The model used for this study is the Community Earth System Model Version 2.2 (CESM2.2; Danabasoglu et al. 2019) developed by the United States of America National Center for Atmospheric Research (NCAR) and Department of Energy

75 (DOE). Three new SE configurations were based on the in-built "F2000climo" AMIP-style configuration (Atmospheric Model Intercomparison Project; Gates, 1992), which uses active components of atmosphere (Community Atmosphere Model; CAM version 6.0), land (Community Land Model; CLM version 5.0), land-ice (Community Ice Sheet Model; CISM 2.0), and river runoff (Model for Scale Adaptive River Transport; MOSART), but has prescribed SSTs. The new configurations continue to use prescribed Sea Surface Temperature (SST) and sea ice concentrations from the in-built CESM file with gx1v7 tri-pole grid

80 (~1° horizontal resolution). This data was merged from the United States of America National Oceanic and Atmospheric Administration (NOAA) Extended Reconstructed Sea Surface Temperature (ERSST; Huang et al., 2017), the Hadley Centre Sea Ice and Sea Surface Temperature data set (HadISST1; Rayner et al., 2003) and NOAA Optimum Interpolation SST version 2 (OISST2, Reynolds et al., 2007). SSTs boundary conditions were maintained at 1° horizontal resolution in this study in order to isolate the effects of increased atmospheric model resolution. CLM used the same horizontal grid as CAM.

85

Figure 1 shows the horizontal grids of the three configurations used in this study. Figure 1a shows "ne30", which is approximately 1° globally, and will be termed "ne30". However, it differs from the normal CESM ne30 in that one of the projected cube faces have been rotated to be centred over (135°E, 30°N) in the western Pacific. Figure 1b shows "ne30×2", with the western Pacific face refined to approximately 0.5°. Figure 1c shows "ne30×4", with the western Pacific face refined

90 the grid to approximately 0.25°. The ne30×2 and ne30×4 grids have the same refinement region centred at (135°E, 30°N). The process of creating the configurations is described with greater detail in Appendix A.

Thirty years of simulation were carried out for each configuration. Judging from the global mean top of atmosphere net radiation flux, the simulations have effectively reached equilibrium after the first simulated year. However, to ensure that the

95 evaluation of done closer to equilibrium, only the last 20 years of each simulation were used. Model level variables were interpolated to pressure levels using the NCAR Command Language (NCL, 2019). Six-hourly sea-level pressure, vector wind at 850 hPa and 10 m, temperature at 300 hPa, 400 hPa, and 500 hPa were used. Variables in the refinement region were interpolated bilinearly from ne30, ne30×2 and ne30×4 grids onto uniform 1°, 0.5°, and 0.25° latitude-longitude grids, respectively.
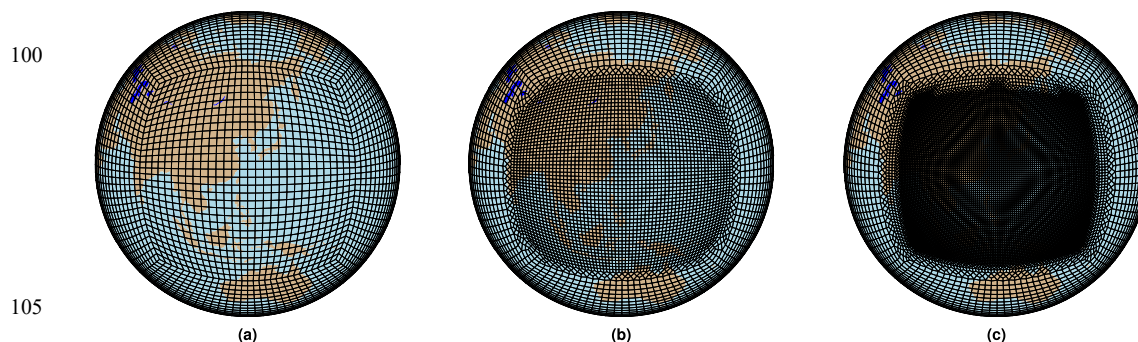
Figure 1. Meshes used in the three SE configurations studied. (a) "ne30", of approximately 1° horizontal resolution; (b) "ne30×2", with mesh refinement over the Asia-Pacific to 0.5°; (c) "ne30×4", with mesh refinement over the Asia-Pacific to 0.25°. (Each element shown in the above figures contains 3×3 collocation cells.)

2.2 Verification Data

Tropical Cyclone (TC) observations were provided by The International Best Track Archive for Climate Stewardship version 4 (IBTrACS v4r00; Knapp et al., 2018). IBTrACS contained data from different sources, and this study used the ten-minute maximum sustained wind speed and TC tracks from the World Meteorological Organisation (WMO). The horizontal resolution was 0.1° (~10 km), and temporal resolution was 6-hourly at 00, 06, 12 and 18 hours UTC. The classification guidelines from the China Meteorological Administration (Table 1) were used to group the TCs of the 2001–2020 period into four categories of "Super Typhoon" (SPTY), "Severe Typhoon" (STY), "Typhoon" (TY) and "TCs weaker than Typhoon" (<TY). During the 2001–2020 period, 18% of the recorded systems were missing wind speeds (5.45 systems per year on average), and these were not used in the analysis.

The typhoon tracking algorithm used in this study was first tested on the European Centre for Medium-Range Weather Forecasts (ECMWF) atmospheric reanalysis version 5 (ERA5; Hersbach et al., 2020), before being applied to the model output. The native ERA5 grid was the reduced gaussian grid N320 (~31 km), but the 0.25°-interpolated version was downloaded from the Copernicus Climate Change Service (Hersbach et al., 2017). Hourly sea-level pressure (SLP), vector wind at 10 m ($\mathbf{U}10m$) and 850 hPa ($\mathbf{U}850$), temperature at 300 hPa (T300), 400 hPa (T400), and 500 hPa (T500) were downloaded. ERA5 variables were bilinearly interpolated to standard 1°, 0.5°, and 0.25° grids. The exception was $\mathbf{U}850$, where relative vorticity was calculated first calculated then interpolated. The interpolated 850 hPa relative vorticity ($\zeta850$) was then directly used in the detection algorithm described in Section 2.3. To match the temporal resolution of the SE simulation output, the hourly data

was averaged every six times steps in ranges of 00–05, 06–11, 12–17, and 18–23 H UTC, then recorded to 00, 06, 12 and 18H

130   UTC, respectively. The choice of forward, backward or centred mean probably does not have an effect larger than the

uncertainty resulting from bias correction, as described below.

TCs are classified according to the guidelines of the Chinese Meteorological Administration, which classifies TCs by their

two-minute maximum sustained wind speed (MSW) as shown in Table 1, so the 6-hourly mean wind speeds from ERA5 and

135   the SE simulations had to be bias corrected to equivalent values. The more accurate description of "scale conversion" will be

used for this process henceforth in the manuscript. The authors decided to convert the 6-hourly wind speeds into *10-minute*

MSW as following WMO standards, but classify the *10-minute* MSW according to the CMA classification which was based

on 2-minute MSW. This was so that TCs be more re-classified and compared to TC data of the Hong Kong Observatory and

Japan Meteorological Agency, both of which use 10-minute MSW, without recalculating wind speeds. TCs in IBTrACS were

140   similarly classified according to their 10-minute MSW from the WMO category, but comparison between WMO and CMA

classifications showed no differences. Knapp and Kruk (2010) provided scale conversion factors between different MSW of

different averaging periods. Harper et al. (2010) proposed guidelines for converting TC winds between different averaging

periods through multiplication by the appropriate scaling factors, but did not provide a factor for converting between 6-hour

mean and 10-minute maximum wind speeds. The gradients from the linear regression of IBTrACS maximum sustained wind

145   speeds against ERA5 10 m wind speeds collected from all matching TCs were used as scale conversion factors. This was

performed three times for each horizontal resolution, but the authors found that the same conversion factor sufficed for the

three resolutions.

Table 1. Classification guidelines used by the China Meteorological Administration. "MSW" stands for the 2-minute

150   maximum sustained surface wind speed near the storm centre. TD, TS, and STS were considered as a single category of

"Tropical Storm or Depression" (<TY) in this study.

CMA Classification	Full name	MSW (m/s)	Group name in this study	Group label in this study
TD	Tropical Depression	10.8 – 17.1	TCs weaker than Typhoon	<TY
TS	Tropical Storm	17.2 – 24.4		
STS	Severe Tropical Storm	24.5 – 32.6		
TY	Typhoon	32.7 – 41.4	Typhoon	TY
STY	Severe Typhoon	41.5 – 50.9	Severe Typhoon	STY
SPTY	Super Typhoon	≥ 51.0	Super Typhoon	SPTY

2.3 Typhoon tracking algorithm

155 Algorithms used to identify TCs commonly apply thresholds to relative vorticity, wind speed, and/or temperature, the last of which is used to detect for the "warm core" of a TC. The "storm centre" is typically defined to be location of the lowest sea-level pressure closest to identified TC. Haarsma et al. (1993) and Bengtsson et al. (1995) used the threshold of 3.5×10^{-5} s^{-1} for relative vorticity at 850 hPa ($\zeta850$), as well as a life-time threshold of 3 days and 1.5 days, respectively. Many studies used a surface or near-surface wind speed threshold of around 17 m s^{-1} to limit the detection to systems of tropical storm intensity or

160 greater, such as Broccoli and Manabe (1990), Wu and Lau (1992), Haarsma et al. (1993) and Vitart et al. (1997). Zhao et al. (2009) and Li et al. (2021) differentiated TCs with warm cores from extra-tropical cyclones, by setting a 1 K minimum threshold for mean temperature anomaly in the upper troposphere (500–300 hPa). Knutson (2007), and Zarzycki and Jablonowski (2014) additionally stipulate that the maximum $\zeta850$ and the warm core must be close to the storm centre, using threshold limits in the range 2°–4°. There appears no hard rule on the exact threshold values used, with different studies

165 adjusting relative vorticity and/or wind speed thresholds in accordance to the model resolution or the study's specific needs (Camargo and Zebiak, 2002). Indeed, some studies have recommended that the vorticity threshold be increased as the model resolution increased, such as Knutson et al. (2007), Zhao et al. (2009), Zarzycki and Jablonowski (2014). Following Bengtsson et al. (1995), this study used relative vorticity and surface wind thresholds of 3.5×10^{-5} s^{-1} and 15 m s^{-1}, respectively.

170 The typhoon tracking algorithm used in this study was mainly scripted with NCL, and consisted of three parts: TC identification, track creation, and clean-up. Firstly, candidates for TCs were identified at each time-step of the 6-hourly model output through a spatial search. Secondly, tracks were constructed starting from each TC candidate through a temporal search. Thirdly, duplicate and weak tracks were removed. Before the algorithm could be applied, the model output was pre-processed as described below.

175

2.3.1 Data pre-processing

Vector wind at 10 m ($U10m$) and 850 hPa ($U850$), sea-level pressure (SLP), and temperatures at 300 hPa (T300), 400 hPa (T400) and 500 hPa (T500) over the Western Pacific region of (100–180°E, 0–30°N) were used for typhoon detection. Before the tracking algorithm was applied, these variables from were bilinearly interpolated from the ne30, ne30×2, and ne30×4 grids

180 simulations to uniform 1°, 0.5°, and 0.25° latitude-longitude grids, respectively. Relative vorticity at 850 hPa ($\zeta850$) was then calculated from the interpolated $U850$ using the central difference method (Bluestein, 1992). This differed from the treatment

of ERA5 where $\zeta850$ was interpolated, because it was more difficult to calculate vorticity from the native model grids. The source and target grids were of comparable resolutions in refinement region, so the adjustment was small.

185 Initial tests found that many false positives were found at sea areas near islands with steep terrain, specifically around Taiwan, New Guinea, and Sumatra. This was resolved by applying a nine-point (3×3 box) smoothing to the $\zeta850$ field, followed by masking out land. The mask created was from ERA5-Land (Muñoz-Sabater et al., 2021), which contained non-values over ocean. An instance of the sea-level pressure field at 1° horizontal resolution was downloaded, the land values set to 1, and bilinearly interpolated to 0.5° and 0.25° degrees to create masks for ne30×2 and ne30×4, respectively. The resultant field had

190 the value of 1 over land, and non-value otherwise (ocean and coasts). This was applied in reverse over the $\zeta850$ fields, i.e. relative vorticity was masked out over land, and retained otherwise. For ne30, a mask prepared from 1° ERA-Land was compared with a mask prepared from 2° ERA-Land. The latter seemed to result in better typhoon detection, and was used. ERA-Land was initially used since the typhoon tracking algorithm was tested on ERA5. However, the mask was retained to pre-process CAM-SE output instead of preparing new masks from the land-sea variable of each configuration. This ensured

195 that ERA5 and the CAM-SE output were put through the same algorithm, for comparisons between the two.

2.3.2 Candidate identification

Initial typhoon candidate were identified at each data time step. The grid-point with the maximum $\zeta850$ was found in the (100–180°E, 0–30°N) identification region, defined to be the "vorticity centre". If the maximum $\zeta850$ exceeded the 3.5×10^{-5} s^{-1}

200 threshold, the vorticity centre was recorded as an initial typhoon candidate, and $\zeta850$ within a 6°×6° grid-box centred on the vorticity centre was set to 0. The search was repeated until up to a maximum of 10 initial candidates in the entire analysis region was found. The 6°×6° grid-box was selected after testing four possibilities of 10°×10°, 6°×6°, 5°×5°, and 3°×3°. The number of initial candidates produced was too low using the 10°×10° grid-box, while candidates tended to overlap (belong to the same system) with the 3°×3° grid-box. Similar to Zhao et al. (2009) which used grid-box of 6°×6°, the authors found 6°×6°

205 or 5°×5° was optimal, with little difference between the two in terms of candidates extracted. The limit of 10 increased the algorithm speed while including all final typhoon candidates, which were candidates that fulfilled the four "TC criteria" below.

(1) The grid-point with the minimum SLP was found within an 8°×8° grid-box centred on the vorticity centre, defined to be the "storm centre". If the distance between the vorticity maximum and storm centre exceeded 3°, the candidate was

210 discarded. The distance threshold was an intermediate value between previously used values of 2° (Knuston et al., 2007)

and 4° (Zarzycki and Jablonowski, 2014). The authors found that the use of 2° falsely eliminated some weak systems, while the use of 4° resulted in more duplicate trajectories.

(2) If maximum |$\mathbf{U}$10m| within an 8°×8° grid-box centred on the storm centre did not exceed 15 m s^{-1}, the candidate was
215   discarded. The 8°×8° grid-box was used because observed maximum surface wind speeds typically occur within 100-400 km of storm centres. The six-hourly wind speed was scale converted before this criterion was applied.

(3) The mean of temperatures at T500, T400 and T300 was taken to produce T. The grid-point with the maximum T (T_{MAX}) was found within an 8°×8° grid-box centred on the storm centre, defined to be the "warm core". If the distance between
220   the warm core and the storm centre exceeded 2°, the candidate was discarded.

(4) Let T_{AVE} be the mean T within an 8°×8° grid-box centred on the warm core. If $T_D = T_{MAX}$-T_{AV} was greater than 1 K, the system was a TC (Zhao et al., 2009; Li et al., 2021). Otherwise, the candidate was discarded as an extra-tropical cyclone. Besides the threshold of 1 K, various thresholds values of 0.8–1.2 K were also tested, but there was little impact on the
225   candidates produced. The box choice of 8°×8° was selected after testing a range of values from 4° to 16°. The authors found that the use of 4° falsely eliminated some TCs, while the use of 16° excessively eliminated many TCs.

Criterion (2) involved a surface wind speed threshold, yet the scale conversion factor for wind speed required the TC tracks to first be extracted. This was solved by boot-strapping the TC detection. The tracking algorithm was first applied without
230 criterion (2), and the resultant tracks manually matched to real ones in IBTrACS. The scale conversion factor was calculated, then the tracking algorithm was applied again with criterion (2).

2.3.3 Track creation

Tracks of up to 15 days were created using each final typhoon candidate from Section 2.3.2 as the initial point, which was
235 generally sufficient to cover the lifetime of most typhoons. The track record included a TC flag R(t), which was initialised to be zero, and always true at the initial time-step which began with a final typhoon candidate, i.e. R(t=0)=1. The initial track location $\mathbf{S}$(t=0) was set to the storm centre of the candidate. In extremely rate cases occurring about once every 300 typhoon tracks, two different final candidates produced identically located storm centres. In such cases, the final candidate with smaller relative vorticity was discarded. From there, a track was constructed as described below.

240

For $i < 60$, given the old storm centre $S(t=i-1)$, let the new storm centre $S(i)$ at the next time-step (six hours later) be the grid-point with the minimum SLP within an $8° \times 8°$ grid-box centred on $S(i-1)$, if the distance between new and old storm centres $|S(i) - S(i-1)| \leq 3.5°$. Otherwise, the track was terminated at $S(t=i-1)$. The $8° \times 8°$ grid-box was chosen based on the maximum recorded TC movement speed of 50 km h^{-1} or 300 km in six hours (Super Typhoon Haiyan in 2013). The grid-point with

245 maximum $\zeta 850$ within an $8° \times 8°$ grid box centred on the new storm centre $S(i)$ was found, i.e. the vorticity centre. If the maximum $\zeta 850$ exceeded the 3.5×10^{-5} s^{-1} threshold and the T criteria were fulfilled, the TC flag was set to true, i.e. $R(i) = \max(R) + 1$. Otherwise, the location of the system was recorded but the TC flag remained false, i.e. $R(i) = 0$.

2.3.4 Track clean-up

250 Section 2.3.2 produced on average around 600 tracks $S_k(t=0...59)$ per year for ERA5 and ne30×4, with $k=1...K$ denoting the kth of K total tracks produced for that year. This naturally includes duplicate tracks, because each track was constructed starting from a final typhoon candidate. The tracks were first filtered according to the following rules:

(1) Tracks were discarded if the system entered the southern hemisphere.

255

(2) The portion of a track after landfall was discarded. Since $\zeta 850$ over land was set to non-values, landfall time was defined to be t_F when the search for maximum $\zeta 850$ around $S(t_F)$ returned a non-value.

(3) Tracks were discarded if they were excessively weak in the first four days, i.e. $\max[R(t \leq 15)] = 1$ where only $R(0)$ was a

260 final candidate from Section 2.3.2. During initial testing of the algorithm, comparison between tracks derived from ERA5 and IBTrACS indicated that other weak low-pressure systems were being connected to the real typhoons, then erroneously counted as typhoons. The removal of weak tracks partly prevents this problem. The choice of four days (16 timesteps) was selected after testing a range of 3–5 days (12–20 timesteps). This rule was not applied during the boot-strap of the scale conversion factor, because weak systems could not be properly determined without criterion (2) of Section 2.3.2.

265

(4) Tracks were discarded if they fulfilled the TC criteria for less than three days (12 timesteps), i.e. $\max(R) \leq 12$

Finally, duplicate tracks were discarded. A search was conducted such that if the distance between the *p*th track at time-step *m* and the *q*th track at time-step *n*, $|\mathbf{S}_p(m) - \mathbf{S}_q(n)| \leq 3°$, the two tracks were considered duplicates. The duplicate track with a

270   later initialisation time was discarded.

3 Results and Discussion

3.1. Verification of tracking algorithm and scale conversion

275   Verification of the algorithm was carried out for the 2011–2020 period by applying it to the 0.25° ERA5, then comparing the detected tracks (a total of 239 systems detected) with IBTrACS. For example, the results of the algorithm before scale-conversion for years 2017 and 2018 are shown in Figure 2. In this period, IBTrACS recorded 131 TCs that reached or exceeded typhoon intensity (henceforth just "typhoons") inside the identification region. When tracks from ERA5 were manually matched to those in IBTrACS, matches were found for 123 typhoons, or 94% of the IBTrACS total. Five of the six typhoons

280   that were generated east of 180 °E and later moved into the identification region were detected by the algorithm. The sixth (17th TC of 2018) was eventually discarded due to its short-lived and weak track. While the algorithm effectively identified and tracked typhoons, it performed less well for TCs of below typhoon intensity. If TCs of below typhoon intensities were included, the algorithm detected 204 of 262 systems, or 78% of the IBTrACS total. The false alarm of the algorithm was about 15% (35 of 239 detected systems). The ERA5 6-hourly mean wind speeds were understandably much weaker than the

285   maximum sustained wind speeds (MSW) recorded in IBTrACS.

After the first boot-strap round of TC detection, 4365 pairs of IBTrACS MSW and 0.25° ERA5 maximum 6-hourly mean 10 m wind speeds $|\mathbf{U}10m|$ were extracted from the 204 manually matched systems of tropical storm intensity or stronger, i.e. IBTrACS MSW $\geqslant 17.2$ m s^{-1} (Table 1). IBTrACS MSW was linearly regressed against $|\mathbf{U}10m|$, producing a regression

290   coefficient 1.66±0.03 (standard deviation). The same procedure was repeated using ERA5 regridded to 0.5° and 1°, producing regression coefficients of 1.60±0.03 and 1.57±0.04, respectively. If a single scale conversion factor had to be chosen, it should be in the range of 1.6-1.7. The final detection algorithm with scale conversion of $|\mathbf{U}10m|$ and TC criterion (2) was applied to ERA5 and SE simulations. The results are shown in Table 2 and Figures 3a–c. In the discussion that follows, values are considered different if their ranges extended by standard deviation do not overlap.

295

From IBTrACS, the mean annual frequency in each TC category seemed relatively stable for two periods of 2001–2020 and 2011–2020 (row 1 vs row 2 of Table 2). The frequencies for ERA5 estimated by the detection algorithm lay within observed ranges for each TC category (row 3 vs row 2 of Table 2), verifying the general applicability of the algorithm. However, the ERA frequency for the "Super Typhoon" (SPTY) seemed low in the acceptable range for a reanalysis. Nevertheless, it did not

300   seem advisable to increase the scale conversion factor, since comparison of individual pairs of matching paths indicated that some low-intensity systems (<TY) were erroneously scaled into "Typhoon" (TY) or "Severe Typhoon" (STY) intensity. Linear scale conversion is probably less inaccurate at the low and high end of intensities.

305

310

315
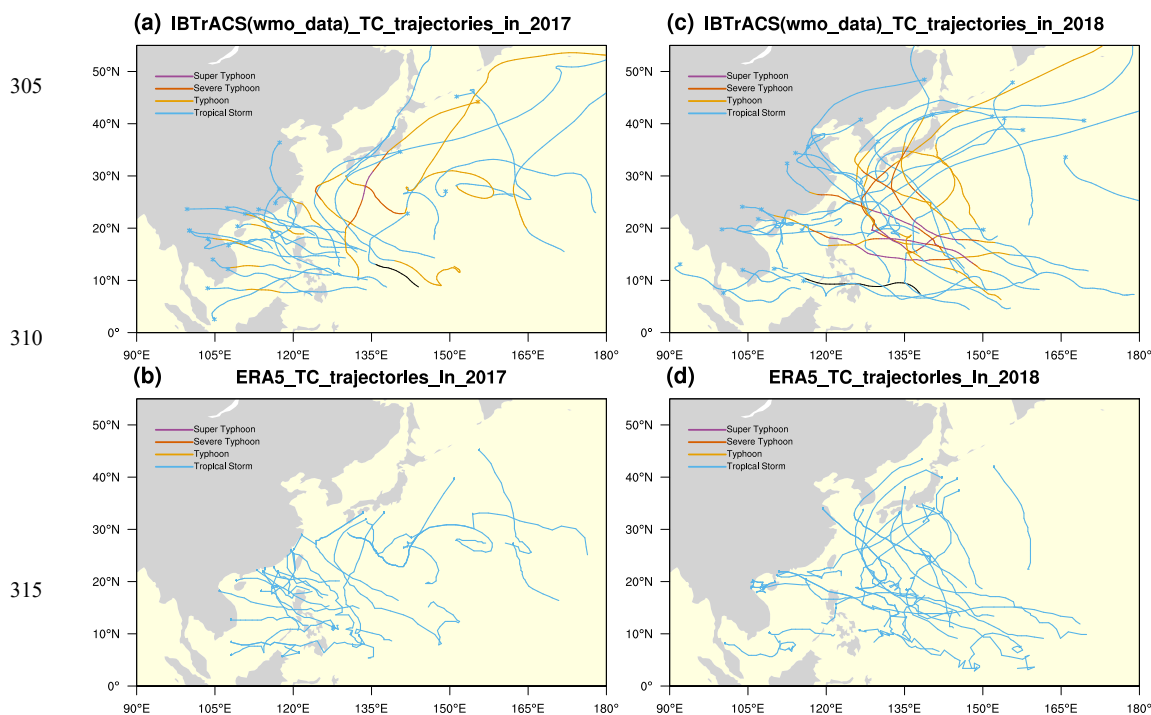
Figure 2. TC tracks of (a) IBTrACS in 2017; (b) 0.25° ERA5 in 2017; (c) IBTrACS in 2018; (d) 0.25° ERA5 in 2018.

320

Table 2. TCs (number/year) using different data sources, with the range calculated from using a scaling correction factor of 1.6 or 1.7, and the larger standard deviations in parentheses. IBTrACS also records systems with missing wind speeds, on the average of about 5 systems per year, which is indicated by "+5" in the first two rows. Bolded values indicate under-estimation.

row	Data source	Period	TC intensity category				Total
			<TY	TY	STY	SPTY	
1	IBTrACS	2001–2020	12 (3)	5 (2)	4 (2)	4 (3)	25 (4) + 5
2		2011–2020	13 (3)	5 (3)	3 (2)	5 (3)	27 (4) + 5
3	0.25° ERA5	2011–2020	8–10 (4)	9 (2)	5–6 (3)	0.5–1 (1)	25 (6)
4	ne30	20 years equilibrium simulation	**4 (2)**	**1 (1)**	**0.3–0.4 (0.6)**	**0**	**5–6 (2)**
5	ne30×2		9–11 (3)	4–6 (2)	2–3 (2)	1 (1)	**18–19 (4)**
6	ne30×4		13 (4)	6 (3)	3–4 (3)	4 (2)	26–28 (7)
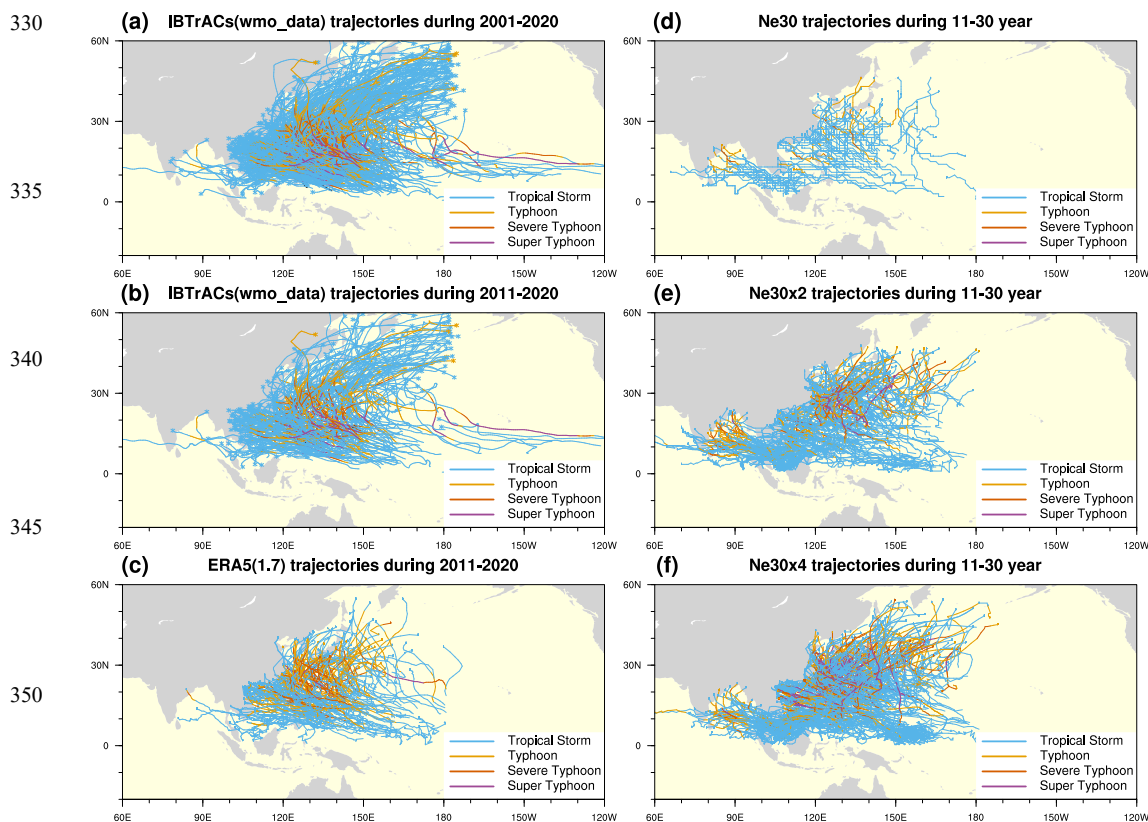
Figure 3. TC tracks from (a) IBTrACS for the period of 2001–2020; (b) IBTrACS for the period of 2011–2020; (c) ERA5 for the period of 2011–2020; (d) ne30; (e) ne30×2; (f) ne30×4. A scale conversion factor of 1.7 was used for panels (c)–(f).

3.2 Typhoon statistics in CAM-SE

3.2.1 Typhoon tracks

Rows 4–6 in Table 2 show the mean annual frequency in each TC category estimated for the SE simulations. The ne30 configuration was poor at producing TCs, and underestimated frequencies in all categories (row 4 of Table 2). The underestimation was more severe for more intense categories, with almost no Severe Typhoons or Super Typhoons. The frequency of all TCs was only about a sixth of observed. In contrast, the frequencies estimated for ne30×2 lay within observed ranges for individual intensity categories (row 5 for Table 2). However, the ne30×2 values fell on the low end on the observed range, particularly for low-intensity systems (<TY) and Super Typhoons. This resulted in the total frequency falling below the observed range; from Table 1, 14–23 systems per year of row 5 compared 26–34 systems per year of row 1. Of the three SE simulations, ne30×4 was clearly the best at producing TCs. The frequencies estimated for ne30×4 lay within observed ranges for all categories (row 6 for Table 2).

Figures 3d–3f show the TC tracks detected in ne30×4, ne30×2 and ne30. The regions of peak intensity were similarly located compared to the region in ERA5 for the period of 2011–2020 (Figure 3c), at approximately 120–150°E, 15–40°N. The ERA5 region was located to the north of that in IBTrACS for the same period (Figure 3b), at approximately 120–150°E, 5–30°N. The region in IBTrACS for the two periods of 2001–2020 and 2011–2020 were similarly located (Figures 3a and 3b), so the observed region of peak intensity appeared stable over time. Instead, ERA5 and the SE simulations were either inherently spatially biased, or the scale conversion process had caused this bias.

Figure 4 shows the differences in track densities between different data source. Figures 4a–c indicate while the ability to simulate enough TCs improve with increasing SE spatial resolution, the spatial biases in track location remain largely similar between the three resolutions with over-estimation of south of 10°N. Most were tracks of low-intensity systems (Figures 3d–f), and likely false alarms created from multiplication by the scale conversion factor. A more serious issue with respect to the scientific question posed in this study was the under-estimation of tracks passing west of the Philippines into southern China. Figures 4d–e indicate that increasing SE spatial resolution nevertheless improved the spatial bias of excessive tracks over the East China Sea–Yellow Sea–Sea of Japan region (dashed circle). The spatial biases of track location were not unique to the SE simulations. ERA5 showed biases with a spatial distribution similar to the SE simulations, although the biases were much smaller expected for a reanalysis (Figure 4f).
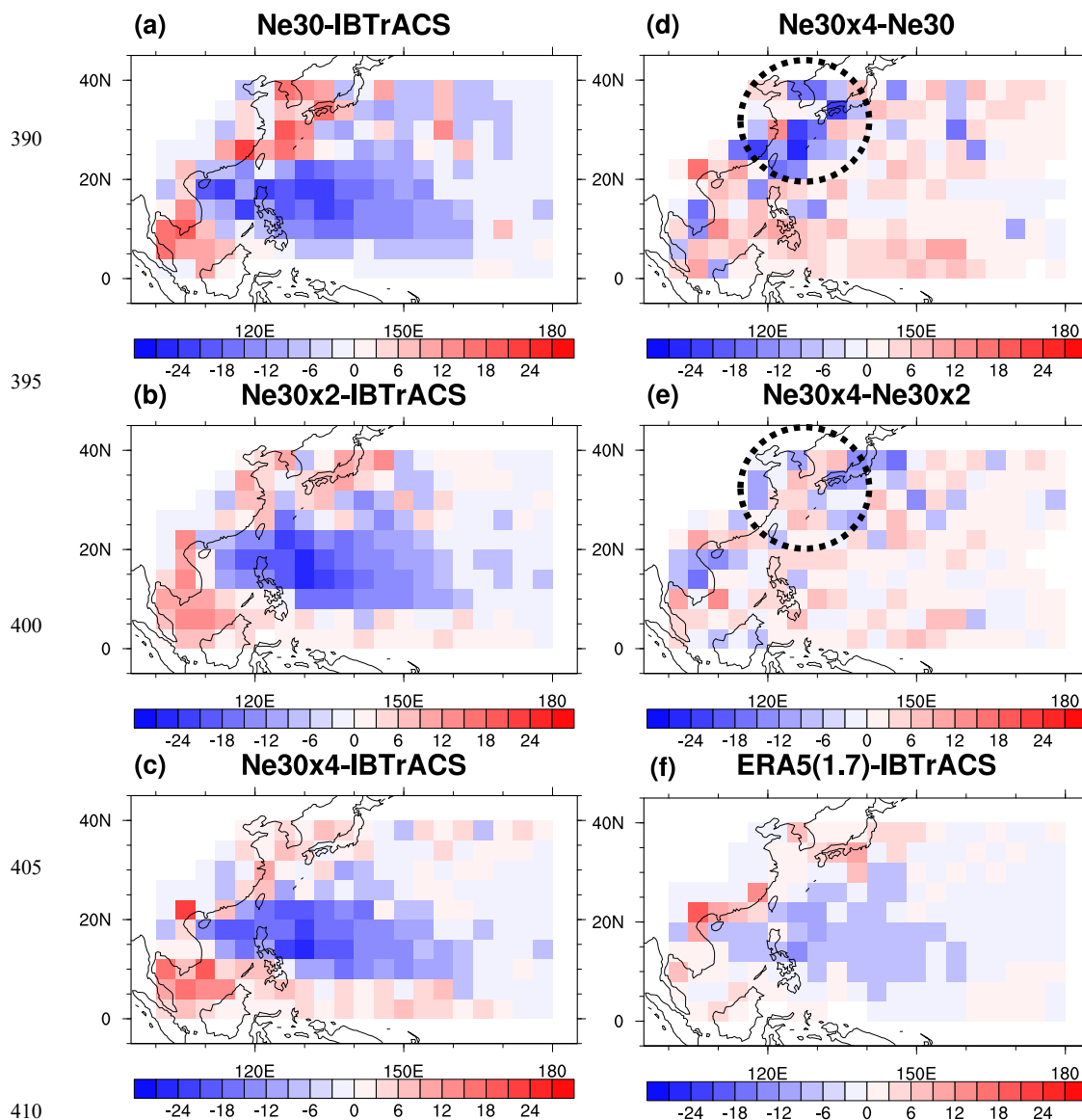
Figure 4. Differences in track density between datasets in units of cyclones per year. The tracks were binned into 4°×4° grid-boxes before differences were taken. (a)–(c) show differences of SE simulations from IBTrACS, i.e. IBTrACS subtracted from SE for (a) ne30; (b) ne30×2; (c) ne30×4. (d)–(e) show the differences of coarser resolution SE simulations from the highest resolution simulation, i.e. ne30×4 subtracted from (d) ne30, (e) ne30×2. Dashed circles indicate the East China Sea–Yellow Sea–Sea of Japan region. (f) The difference of ERA5 from IBTrACS for the period of 2011–2020. The scale conversion factor of 1.7 was used.

3.2.2 Typhoon generation locations

Figures 5a–c show the TC genesis locations in IBTrACS and ERA5. The same main genesis region (105–165 °E, 5–20 °N)

420 was seen in both periods of IBTrACS (Figures 5a and 5b). Few TCs were generated to the north of 25°N during the entire 2001–2020 period, and most were of intensity weaker than "Typhoon". Only one weak system was generated north of 30°N near Japan (Figure 5a). Observed genesis locations of tropical cyclones in the South China Sea were concentrated in the northern part of this area, and most were of intensity weaker than "Typhoon". Only seven typhoons were generated in the South China Sea, and none were severe or Super Typhoons. The TCs genesis locations in ERA5 was similar to that in IBTrACS

425 for the same period (Figure 5c vs 5b), in agreement with the results shown in Figure 2. This verifies the ability of the tracking algorithm to capture genesis locations. Most genesis points in the South China Sea were located in the northern part of the sea, and these corresponded mostly systems of lower intensities. However, systems in ERA5 were biased towards higher intensities. Few genesis points occurred in the East China Sea, indicating that TCs entering these regions were not locally generated.

430 Figures 5d–f show the TC genesis locations in the SE simulations. The main genesis region in ne30×4 had a similar longitudinal span as that in IBTrACS and ERA5, but its latitudinal range extended to 30°N, i.e. the model over-generated TCs at higher latitudes. This phenomenon has also been observed in FGOALS-f3-H (Li et al., 2021) and high-resolution GCMs participated in the European Union Horizon 2020 project PRIMAVERA (Roberts et al., 2020). Genesis points in the South China Sea were mostly in the southern part of the sea. Inspection of the corresponding tracks indicated that these westward into the Bay of

435 Bengal after genesis, and some of them were reached or exceed "Severe Typhoon" intensity. Such systems would be considered to be Indian Ocean TCs by IBTrACS instead, likely accounting for much of the discrepancy of track density over the South China Sea. The number of systems generated in from the Pacific moving westward into the South China Sea were similar with IBTrACS. In the north part of the South China Sea, systems generated near Luzon island were excessively intense. Genesis points in the East China Sea were excessive the along the coast of mainland China and around Taiwan island, compared to

440 observation. Since the genesis locations in ERA5 and IBTrACS were similar, the different genesis locations in the simulations were not caused by the tracking algorithm.

Considering the poorer performance in simulating lower-intensity systems, Figure 6 compares the genesis spatial density for only Super Typhoons. The same main genesis region (125–175°E, 0–25°N) was seen in both periods of IBTrACS, as well as

445 ERA5. The genesis region of ne30×4 still extended further west and north compared to that of IBTrACS (Figure 6b vs 6a). The latitudinal bias may be partly explained by the location of the annual mean subtropical high in the simulations.
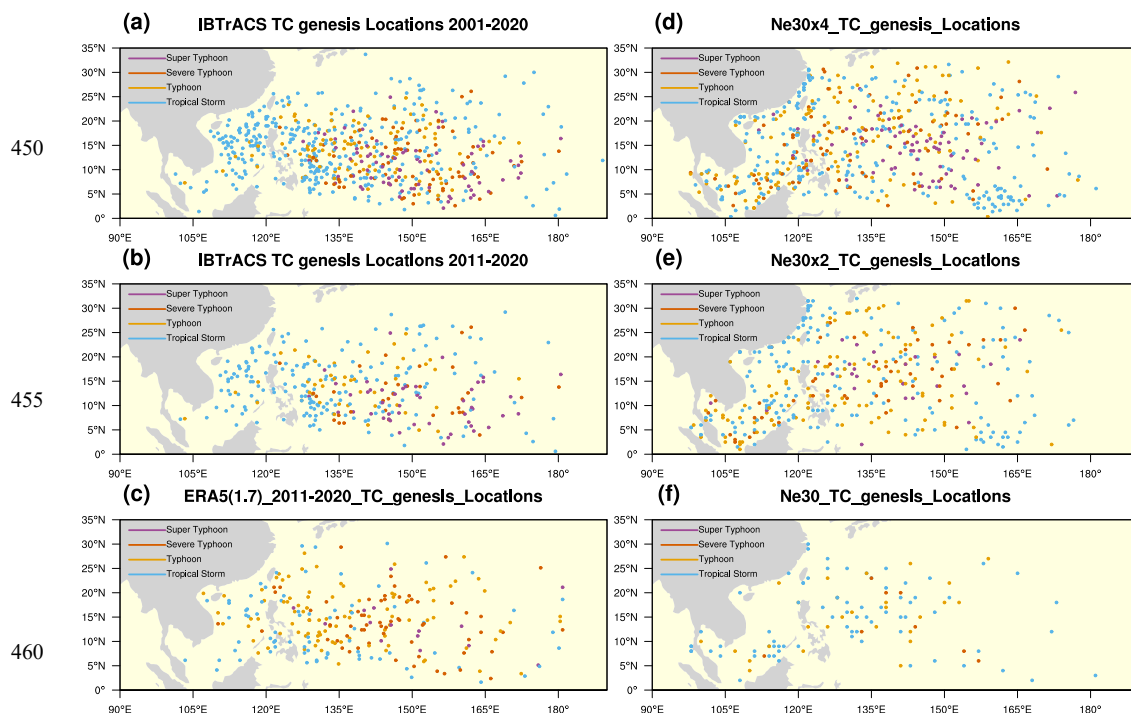
Figure 5. TCs genesis locations in (a) IBTrACS for the period of 2001–2020; (b) IBTrACS for the period of 2011–2020; (c) ERA5 for the period of 2011–2020; (d) ne30×4; (e) ne30×2; (f) ne30. TCs were coloured by the maximum peak intensity during their lifetime. The scale conversion factor of 1.7 was used.
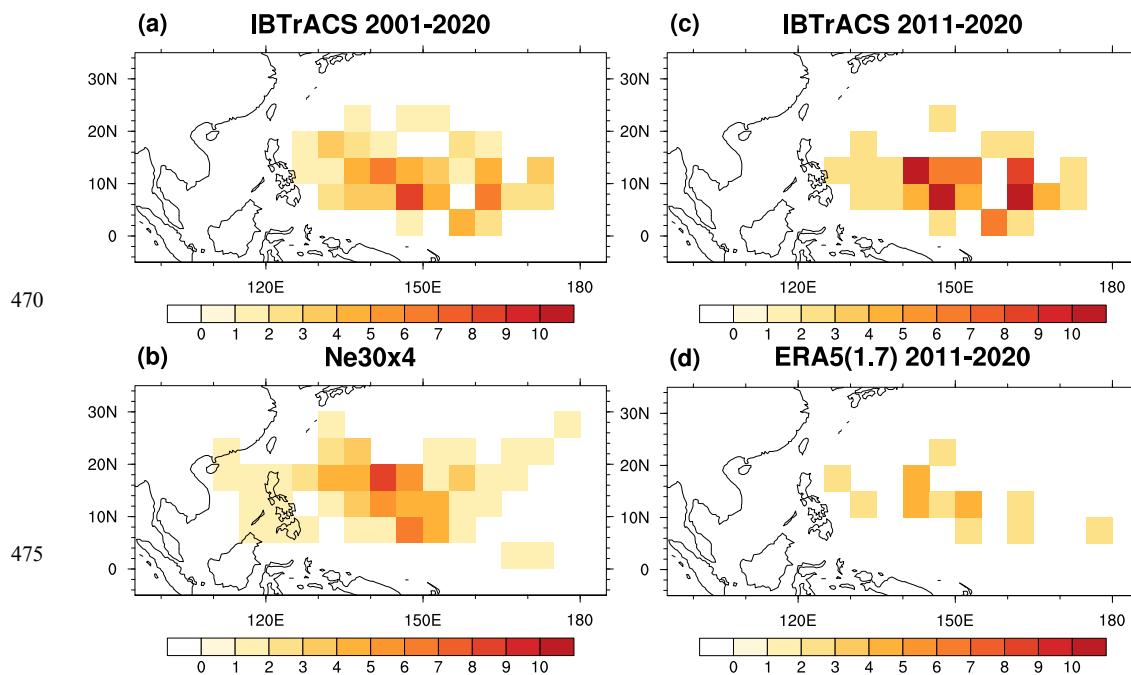
465

Figure 6. Genesis locations of Super Typhoons (multiple 20) in units of number per year, binned into 5°×5° grid-boxes, (a)

IBTrACS for the period of 2001–2020; (b) ne30×4, (c) IBTrACS for the period of 2011–2020, (d) ERA5-1.7: 2011-2020

3.2.3 Typhoon energy and life-span

Accumulated Cyclone Energy (ACE) is a measurement that combines the duration and intensity of TCs (Bell et al., 2000), and is defined as $ACE = 10^{-4} \sum (V_{MAX})^2$, where V_{MAX} is the maximum surface wind speed (knots) of the TC at any given time. ACE was calculated for each TC by summing the square of the maximum 10 m surface wind speed every 6 hours along the track. The results are shown in Table 3.

Based on IBTrACS, the annual ACE in the period of 2001–2020 had a large range of 114–418. However, the mean annual ACE (henceforth just "ACE") for the two periods of 2001–2020 and 2011–2020 was the same at 250±80 (standard deviation). The values for typhoons were also the same for both periods, at 220±80. The 0.25° ERA5 ACE for all systems and typhoons were 270±70 and 230±70, respectively, which fell in the observed range for the same period.

In contrast, the ne30 ACE was clearly to low at 40±10 for all systems, or only 16% of the observed value. The ACE for weaker-intensity (<TY) systems was 20±10, which fell in the observed range of 27±9 (IBTrACS 2001–2020 period); The shortage was from typhoons which also had an ACE of 20±10, only 9% of the observed 220±80. This was no solely due to the smaller number of typhoons produced, since the ACE normalised by number of typhoons (ACE/TC) was only about 60% of the observed value (10 vs 17). The ne30×2 ACE for all systems and typhoons was 180±50 and 130±50, respectively, which fell into the lower end of the observed range. One might expect the ne30×4 to do even better, but this was not the case overall. ACE for all systems was 300±90, which fell into the upper end of the observed range. Further breakdown by TC intensity reveals the problem; Although the ACE for typhoons was 230±80 and closest to the observed range, there ACE for the weaker-intensity systems was 70±20, which fell outside of the observed range. The number of weaker systems produced by ne30×4 was the same as observed, but the ACE/TC in SE simulations were about two times of observed (~5 vs ~2.5). This issue was not unique to the SE simulations, but also present in ERA5, which had a similar ACE/TC value for weak systems. Examination of the lifetime for weaker systems indicated that lifetimes across all data sources lay within the IBTrACS range of 7±3 days (column 1 of Table 4). The mean lifetimes of ne30×2 and ne30×4 were slightly longer by one day (8±4), and which if integrated with the square of the maximum sustained wind, might have resulted in large differences in ACE. These results indicate that care should be taken when dealing with different variables than what one had bias corrected for, i.e. scale conversion was done for wind speed rather than energy. The authors do not consider this discrepancy to be of major concern at this stage of research. Firstly, the study is targeted at typhoons, where the statistics matched observations well. Secondly, least for the SE simulations, the SST was prescribed, and the TC durations are expected to shorten once ocean-interaction is added.

Table 3. Mean annual Accumulated Cyclone Energy (ACE) and ACE normalised by the number of systems, for systems weaker than "Typhoon", typhoons, and all systems. Standard deviations are pended in brackets. The scale conversion factor of 1.7 was used. Bold indicates values that fell outside of the observed IBTrACS range.

Data source	Period	TC intensity category					
		<TY		TY, STY and SPTY		All systems	
		ACE	ACE/TC	ACE	ACE/TC	ACE	ACE/TC
IBTrACS	2001–2020	27 (9)	2.3	222 (81)	17	249 (81)	10
	2011–2020	32 (9)	2.4	218 (81)	17	251 (81)	10
0.25° ERA5	2011–2020	37 (13)	4.9	233 (67)	14	270 (74)	11
ne30	20 years equilibrium simulation	19 (12)	5.1	**18 (11)**	10	**39 (12)**	7
ne30×2		51 (21)	5.5	132 (46)	14	183 (49)	10
ne30×4		**70 (22)**	5.3	229 (84)	16	298 (86)	11

515

Table 4. TCs lifetime in days, for different categories of TC intensity. Standard deviations are pended in brackets. The scale conversion factor of 1.7 was used.

Data source	Period	TC intensity category				All systems
		<TY	TY, STY and SPTY			
			TY	STY	SPTY	
IBTrACS	2001–2020	7 (3)	11 (4)			9 (4)
			10 (3)	12 (4)	13 (4)	
	2011–2020	7 (3)	11 (4)			9 (4)
			9 (3)	12 (4)	12 (4)	
0.25° ERA5	2011–2020	7 (3)	9 (3)			9 (4)
			8 (3)	10 (3)	12 (2)	
ne30	20 years equilibrium simulation	7 (4)	8 (3)			8 (3)
			9 (3)	10 (2)	0	
ne30×2		8 (4)	10 (3)			9 (4)
			9 (4)	10 (3)	10 (3)	
ne30×4		8 (4)	10 (4)			9 (4)
			9 (4)	10 (4)	11 (3)	

520

4.3 Typhoon structure as input for dynamical downscaling

Figure 7 shows the most intense TC generated in each three SE simulations. This reached the peak intensity of only "Severe Typhoon" for ne30, but reached "Super Typhoon" for ne30×2 and ne30×4. The corresponding minimum SLP were 957 hPa, 919 hPa, and 911 hPa for ne30, ne30×2 and ne30×4, respectively (Figurse 7a–c). Estimated maximum sustained wind, or maximum 6-hourly mean |$\mathbf{U}$850|, was 48 m s^{-1}, 60 m s^{-1}, and 72 m s^{-1}, respectively (Figures 7d–e). As expected, ne30×4 produced the most intense TC case.

The most intense TCs in the ne30 and ne30×2 simulation formed on July 25th and July 14th, respectively. Both simulations produced calm typhoon eyes, but the wind speeds were lower over wider areas (Figures 7d, 7e). The eye was not dry in ne30 (Figure 7j), and spiral rain bands were not obvious in ne30×2 (Figure 7k). Nevertheless, the ne30×2 TC seemed generally realistic and still suitable for downscaling.

The most intense TC in the ne30×4 simulation formed over the dense TC genesis area of (150°E,18°N) on September 14th. It then moved westward to near 128°E where it reached it reached its maximum intensity on September 19th, five days after genesis. The TC then moved northward and made landfall on Shikoku island in Japan. Typhoon showed a detailed structure with a distinct eye (Figures 7f, 7i). At this time, the maximum |$\mathbf{U}$850| was located on the east side of the typhoon eye area because the system is moving northward. The spiral rain band was clearly visible, and little precipitation fell over the eye area is the area (Figure 7l).
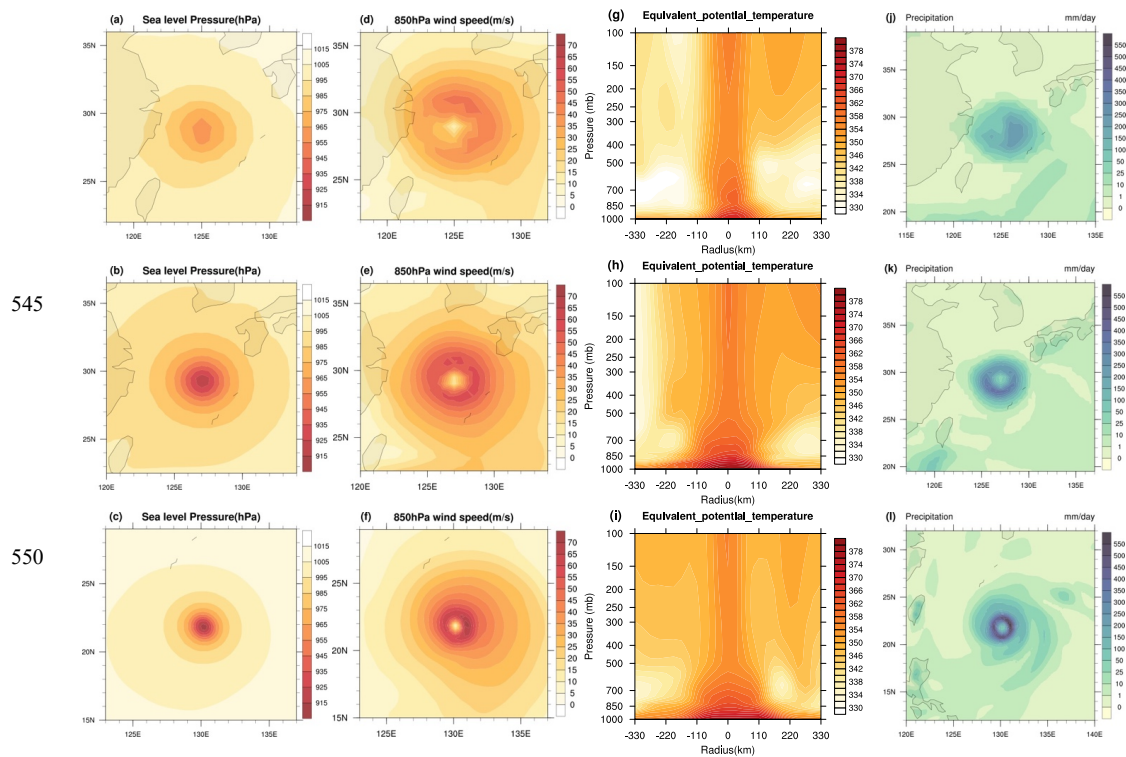
Figure 7. (a)–(c) Sea-level pressure, (d)–(f) 850 hPa wind speed, (g)–(i) longitude-height cross sections of the equivalent potential temperature, and (j)–(l) simulated radar reflectivity, for the most intense storm generated in (top row) ne30, (middle row) ne30×2, and (bottom row) ne30×4.

4.4 Computational efficiency

560   The simulations were carried out on the Tianhe-2 supercomputer at the National Supercomputer Center in Guangzhou, and the computation speeds using different number of processors are shown in Table 5. The computation speeds of three SE configurations were compared with that for the f09 configuration, which uses the finite volume (FV) dynamical core and ~1° global spatial resolution, and the ne120 configuration, which uses the SE dynamical core and ~0.25° global spatial resolution. Although ne120 has about five times the grid-points of ne30×4, the ne30×4 simulation was about nine times faster than the

565   ne120 simulation. This indicated that regionally refined grids were preferable when using the SE dynamical core. At approximately the same 1° spatial resolution, the f09 simulation was about 1.2–1.5 times faster than the ne30 simulation. Hence, there would be no reason to use the SE dynamical core except for its variable resolution capabilities. Assuming that the computation speed of the FV core scaled perfectly by a factor 16 slowdown from 1° to 0.25°, ne30×4 would still be about 2–2.4 times faster than the "perfect" 0.25° FV configuration.

570

Table 5. The computational efficiency of the grids. "f09" refers to the default Finite Volume dynamical core. "ne120" refers to a quasi-uniform SE grid of approximately 0.25° horizontal resolution globally, using default run settings. "N/A" means that the simulation could not execute under the corresponding number of processors.

Grid Name	Approximate resolution (°)	Number of grid-points	processors			
			120	240	480	960
			Simulation speed (model-years per day)			
f09	1	55,296	1.17	2.20	4.10	6.85
ne30	1	48,602	0.78	1.51	2.76	5.60
ne30×2	1 to 0.5	72,326	0.38	0.76	1.46	2.72
ne30×4	1 to 0.25	143,930	0.14	0.28	0.56	1.05
ne120	0.25	777,602	N/A	0.03	0.06	0.11

575

5 Conclusions

The variable resolution capability of the Spectral Element (SE) dynamical core of the Community Atmosphere Model (CAM) was evaluated for Tropical Cyclones (TCs) in the Western Pacific region, to determine if a regionally-refined configuration could produce cost-efficient yet appropriate extreme typhoon statistics for the use of climate studies. Three Asia-centric configurations of CAM-SE were set up. The first had a horizontal resolution of approximately 1° globally, without regional refinement (ne30). The second was regionally refined from 1° to 0.5° over the Asia-Pacific (ne30×2), while the third was regionally refined from 1° to 0.25° (ne30×4). 20 years from equilibrium climate simulations of each configuration were compared with the ERA5 reanalysis and IBTrACS observation record.

To extract TC tracks from the simulations, a tracking algorithm was developed in NCL, and first calibrated on ERA5 reanalysis that had been re-gridded to 0.25°, 0.5°, and 1° spatial resolutions. Scale conversion factors were calculated for converting the 6-hourly mean 10 m wind speeds of the gridded data into 10-minute maximum sustained surface wind speeds (MSW), and classify 10-minute MSW according to the 2-minute MSW used by the China Meteorological Administration to categorise TC intensity. This was done by linearly regressing IBTrACS MSW against between ERA5 mean winds for matching pairs of systems in an initial boot-strap round of the algorithm, to obtain scale conversion factors in the range of 1.6–1.7. The algorithm then repeated on the scaled winds to obtain the final tracks and estimated intensities.

The ne30×4 configuration produced the most realistic statistics for TCs of "Typhoon" or stronger intensities. It was also the only configuration that could generate enough "Super Typhoons", i.e. TCs with maximum sustained central wind speed equal or greater than 51 m s⁻¹. The range of annual "Super Typhoon" generated by ne30×2 was still considered realistic as it fell on the low end of the observed range, but the mean value was too low (1 per year vs observed 4 per year). The improvement of simulated typhoons with the higher resolution is an expected result. However, comparisons of computation speed indicate that the ne30×4 configuration would be at least two times faster than a globally 0.25° configuration using the default finite volume (FV) dynamical core, despite the FV core being faster than the SE core at equivalent global resolutions without regional refinement. Taking into account the overhead of setting up the regionally-refined configurations, such configurations are useful for large experiments requiring many years of simulation, or if computational costs are a concern.

Appendix A: Model setup procedure

Aquaplanet and stability tests

605

The F2000climo configuration which uses the Finite Volume (FV) dynamical core was changed to an aquaplanet with prescribed the zonally symmetric "CONTROL" SST profile of the Aquaplanet Experiment (Neale and Hoskins, 2000), and a simulation using the "f09" grid (~1° horizontal resolution) was produced for comparison against reference outputs (Williamson et al., 2012). The dynamical core was then changed to the SE core, and simulations were produced using both the original

610 ne30 grid, as well as a ne30 grid with one cube face rotated over Asia-Pacific (just "ne30" henceforth. The output regridded to the f09 grid for comparison. A number of refined grids were then created (c.f. the description on grid generation" below), and test simulations were carried out using different values of SE paramerisations. To run refined meshes, the namelist option "se_refined_mesh" option must be set to "True". A new simulation using the ne30 grid also produced with this option on, to send it through the same mesh adjustment of the grid by the model. The refined simulations were compared against the f09

615 and ne30 results. Unstable simulations that could not complete were naturally rejected, as were simulations that produced excessive numerical artefacts or oscillations.

The parameters that were changed are shown in Table A1, namely physics time step, se_nsplit, and se_rsplit. The other SE parameters remained at the CAM's default. The physics time step in all the simulations were set to 1800s, instead of the 0.5°

620 default of 900s and 0.25° default of 450s. This produced no obvious ill-effects, at least at this stage in testing, but was important for improving computation speed. There appears to be a good basis for this selection; Williamson (2013) demonstrated that deep convection scheme in CAM becomes almost inactive at short physics time steps, while Reed et al. (2012) pointed out that a physics time step of 1800s resulted in a more reasonable portioning of convective and large-scale precipitation, and hence more realistic intensities of tropical cyclones. The other parameters that were changed were the sub-cycling parameters

625 se_nsplit and se_rsplit, which were adjusted to stabilise the simulation (Lauritzen et al., 2018). Ideally, ne30 and ne30×2 should be tested using the same sub-cycling parameters as ne30×4, but this was not done due to resource constraints. The differences most probably would not affect the results of this study, but more care should be taken in the future regarding the possible effects of unequal parameters, and ensure that different configurations were as similar as possible except for horizontal resolution.

630

After the grids were finalised, the configurations were returned to land-containing versions. For SST, mapping files that specified the interpolation weights from the gx1v7 tri-pole grid input to the SE grid were created using the "gen_domain" tool

provided in the CESM source code. This file was used by the coupler to provide boundary conditions to CAM during the

simulation. The creation of land topography is described in the "Topography" section below. The initial conditions for the land

635   and atmosphere models were interpolated from that of the original F2000climo configuration using the "VRM_tools" toolkit

provided by NCAR. (These were "warm start" simulations as opposed to the "cold start" aquaplanet simulations.)

Table A1. Namelist parameters setting in the three simulations

	Configuration		
Settings	**ne30**	**ne30×2**	**ne30×4**
dtime	1800s	1800s	1800s
se_nsplit	3	5	6
se_rsplit	3	3	4
se_qsplit	1 (default)		
se_hypervis_power	0 (default)		
se_hypervis_scaling	3.0 (default)		
se_hypervis_subcycle	3 (default)		
se_hypervis_subcycle_q	1 (default)		
se_hypervis_subcycle_sponge	1 (default)		
se_nu	-1 (default)		
se_nu_div	-1 (default)		
se_nu_top	1.0×10^5 (default)		

640

Grid generation

The grids could be generated in two ways, the first with the CUBIT toolkit developed by the Sandia National Laboratory

(Anderson et al., 2009) or the "high-connectivity" method, and the second with the SQuadGen toolkit (Ullrich, 2014) or the

"low-connectivity" method. Guba et al. (2014) compared the two methods, and concluded that the low-connectivity method

645   generated relatively less distorted quadrilateral grids. Grids using both methods were generated with the Community Mesh

Generation Toolkit developed by Earth System Model Computational Infrastructure (ESMCI) in the aquaplanet testing stage.

We decided to use the low-connectivity method because the output fields appeared relatively smoother compared to the high-

connectivity method.

Topography

650   Three different topography-generating methods were tested, the first using bilinear interpolation from the CESM-provided

ne120 grid with approximately 0.25° horizontal resolution, the second using conservative interpolation instead, and the third

using NCAR's TOPO software. Output fields such as the annual climatology of precipitation and surface temperature were

compared between SE simulations and the original f09 simulation. The bilinearly-interpolated topography produced fields

closer to the f09 simulation compared to the conservatively-interpolated topography. At the time of this study, the TOPO

655   toolkit was still under development, and we excluded its use because its output topography might still change during the

development process. The topography produced by bilinear interpolation was not smoothed, and this seemed to cause some

difference with actual topography over steep areas, such as the foothills of the Tibetan Plateau and New Guinea. The

differences most probably would not affect the results of this study, which was focused over oceanic regions. For studies over

orographically diverse regions, it would be advisable to carefully consider the production of topography its impact on the

660   simulation.

Code availability

All software used to process the data are publicly available from their respective project webpages. CESM2 is available at https://www.cesm.ucar.edu/.

Data availability

665

IBTrACS is available at https://www.ncei.noaa.gov/products/international-best-track-archive. ERA5 can be accessed from https://www.ecmwf.int/en/forecasts/dataset/ecmwf-reanalysis-v5. The data and grids described in the study will be made available after the publication of the manuscript.

Author contribution

670

Zheng: Data curation, methodology, investigation, software, visualization, writing. Lee: Conceptualization, supervision, methodology, writing. Lin: Visualization. Ran: Writing. Dong: Resources.

Competing interests

The authors declare that they have no conflict of interest.

Acknowledgements

675

This work was supported by the National Natural Science Foundation of China's Research Fund for International Young Scientists grant number 41950410568, and Japan Ministry of Education, Culture, Sports, Science and Technology Program for the Advanced Studies of Climate Change Projection (SENTAN) grant number JPMXD0722678534. The CESM project is supported primarily by the National Science Foundation (USA). The authors would like to thank all the scientists, software engineers, and administrators who have contributed to the development of CESM 2.2 and the CAM-SE dynamical core. We

680

would also like to thank professor C.L. Wu for patiently answering our many technical questions about CAM-SE setup. Thanks for the support of Tianhe-2 supercomputers at the National Supercomputer Center in Guangzhou.

References

Anderson, B. D., Benzley, S. E., and Owen, S. J.: Automatic all quadrilateral mesh adaption through refinement and coarsening, Proc. 18th Int. Meshing Roundtable, IMR 2009, 557–574, https://doi.org/10.1007/978-3-642-04319-2_32, 2009.

685

Bell, G. and Chelliah, M.: The 1999 North Atlantic and east- ern North Pacific hurricane season [in "Climate Assess- ment for 1999"], B. Am. Meteorol. Soc., 81, S19–S22, https://doi.org/10.1175/1520-0477-80.5s.S1, 2000.

Bengtsson, L., Botzet, M., and Esch, M.: Hurricane-type vortices in a general circulation model, Tellus A, 47, 175–196, 690   https://doi.org/10.1034/j.1600-0870.1995.t01-1-00003.x, 1995.

Bluestein, H.B.: Synoptic-Dynamic Meteorology in Midlatitudes. Oxford University Press, 1992

Broccoli, A. J. and Manabe, S.: Can existing climate models be used to study anthropogenic changes in tropical cyclone 695   climate?, Geophys. Res. Lett., 17, 1917–1920, https://doi.org/10.1029/GL017i011p01917, 1990.

Camargo, S. J. and Zebiak, S. E.: Improving the detection and tracking of tropical cyclones in atmospheric general circulation models, Weather Forecast., 17, 1152–1162, https://doi.org/10.1175/1520-0434(2002)017<1152:ITDATO>2.0.CO;2, 2002.

700   Chan, P. W., He, Y. H., and Lui, Y. S.: Forecasting Super Typhoon Saola and its effects on Hong Kong, Weather, https://doi.org/10.1002/wea.4569, 2024.

Choy, C. W., Lau, D. S., and He, Y.: Super typhoons Hato and Mangkhut , part I: analysis of maximum intensity and wind structure, Weather, 77, 314–320, https://doi.org/10.1002/wea.3797, 2022.

705

Danabasoglu, G., and Coauthors.: The Community Earth System Model Version 2 (CESM2), J. Adv. Model. Earth Syst., 12, 1–35, https://doi.org/10.1029/2019MS001916, 2020.

Dennis, J., Fournier, A., Spotz, W. F., St-Cyr, A., Taylor, M. A., Thomas, S. J., and Tufo, H.: High-Resolution Mesh 710   Convergence Properties and Parallel Efficiency of a Spectral Element Atmospheric Dynamical Core, Int. J. High Perform. Comput. Appl., 19, 225–235, https://doi.org/10.1177/1094342005056108, 2005.

Dennis, J. M., Edwards, J., Evans, K. J., Guba, O., Lauritzen, P. H., Mirin, A. A., St-Cyr, A., Taylor, M. A., and Worley, P. H.: CAM-SE: A scalable spectral element dynamical core for the Community Atmosphere Model, Int. J. High Perform.

715   Comput. Appl., 26, 74–89, https://doi.org/10.1177/1094342011428142, 2012.

Devanand, A., Huang, M., Lawrence, D. M., Zarzycki, C. M., Feng, Z., Lawrence, P. J., Qian, Y., and Yang, Z.: Land Use and Land Cover Change Strongly Modulates Land-Atmosphere Coupling and Warm-Season Precipitation Over the Central United States in CESM2-VR, *J. Adv. Model. Earth Syst.*, 12, 1–23, https://doi.org/10.1029/2019MS001925, 2020.

720

Gates, W. L.: AMIP: the Atmospheric Model Intercomparison Project, Bull. - Am. Meteorol. Soc., 73, 1962–1970, https://doi.org/10.1175/1520-0477(1992)073<1962:ATAMIP>2.0.CO;2, 1992.

Guba, O., Taylor, M. A., Ullrich, P. A., Overfelt, J. R., and Levy, M. N.: The spectral element method (SEM) on variable-

725   resolution grids: Evaluating grid sensitivity and resolution-aware numerical viscosity, Geosci. Model Dev., 7, 2803–2816, https://doi.org/10.5194/gmd-7-2803-2014, 2014.

Haarsma, R. J., Mitchell, J. F. B., and Senior, C. A.: Tropical disturbances in a GCM, Clim. Dyn., 8, 247–257, https://doi.org/10.1007/BF00198619, 1993.

730

Harper, B. A., Kepert, J. D., and Ginger, J. D.: Guidelines for converting between various wind averaging periods in tropical cyclone conditions, World Meteorological Organisation, 2010.

Hersbach, H., and Coauthors.: Complete ERA5 from 1940: Fifth generation of ECMWF atmospheric reanalyses of the global

735   climate. Copernicus Climate Change Service (C3S) Data Store (CDS), https://doi.org/10.24381/cds.143582cf (Last accessed: 20-May-2024), 2017.

Hersbach, H., and Coauthors.: The ERA5 global reanalysis, Q. J. R. Meteorol. Soc., 146, 1999–2049, https://doi.org/10.1002/qj.3803, 2020.

740

Huang, B., and Coauthors.: NOAA Extended Reconstructed Sea Surface Temperature (ERSST), Version 5, NOAA National Centers for Environmental Information, https://doi.org/10.7289/V5T72FNM, 2017.

Huang, X. and Ullrich, P. A.: Irrigation impacts on California's climate with the variable-resolution CESM, *J. Adv.*
745 *Model. Earth Syst.*, 8, 1151–1163, https://doi.org/10.1002/2016MS000656, 2016.

Hurrell, J. W., and Coauthors.: The Community Earth System Model: A Framework for Collaborative Research, Bull. Am.
Meteorol. Soc., 94, 1339–1360, https://doi.org/10.1175/BAMS-D-12-00121.1, 2013.

750 Knapp, K. R., and Coauthors.: International Best Track Archive for Climate Stewardship (IBTrACS) Project, Version 4,
NOAA National Centers for Environmental Information, https://doi.org/10.25921/82ty-9e16, 2018.

Knutson, T. R., Sirutis, J. J., Garner, S. T., Held, I. M., and Tuleya, R. E.: Simulation of the Recent Multidecadal Increase of
Atlantic Hurricane Activity Using an 18-km-Grid Regional Model, Bull. Am. Meteorol. Soc., 88, 1549–1565,
755 https://doi.org/10.1175/BAMS-88-10-1549, 2007.

Lauritzen, P. H., and Coauthors.: NCAR Release of CAM-SE in CESM2.0: A Reformulation of the Spectral Element
Dynamical Core in Dry-Mass Vertical Coordinates With Comprehensive Treatment of Condensates and Energy, J. Adv. Model.
Earth Syst., 10, 1537–1570, https://doi.org/10.1029/2017MS001257, 2018.

760

Li, J., Bao, Q., Liu, Y., Wang, L., Yang, J., Wu, G., Wu, X., He, B., Wang, X., Zhang, X., Yang, Y., and Shen, Z.: Effect of
horizontal resolution on the simulation of tropical cyclones in the Chinese Academy of Sciences FGOALS-f3 climate system
model, Geosci. Model Dev., 14, 6113–6133, https://doi.org/10.5194/gmd-14-6113-2021, 2021.

765 Li, Y., Wu, J., Tang, R., Wu, K., Nie, J., Shi, P., Li, N., and Liu, L.: Vulnerability to typhoons: A comparison of consequence
and driving factors between Typhoon Hato (2017) and Typhoon Mangkhut (2018), Sci. Total Environ., 838, 156476,
https://doi.org/10.1016/j.scitotenv.2022.156476, 2022.

Muñoz-Sabater, J., and Coauthors.: ERA5-Land: a state-of-the-art global reanalysis dataset for land applications, Earth Syst.
770 Sci. Data, 13, 4349–4383, https://doi.org/10.5194/essd-13-4349-2021, 2021.

Murakami, H. and Sugi, M.: Effect of Model Resolution on Tropical Cyclone Climate Projections, SOLA, 6, 73–76,
https://doi.org/10.2151/sola.2010-019, 2010.

775   Neale, R. B., and B. J. Hoskins: A standard test for AGCMs including their physical parametrizations. I: The proposal. *Atmos.*
        Sci. Lett., **1**, 101–107, https://doi.org/10.1006/asle.2000.0019, 2000.

        Neale, R. B., and Coauthors.: Description of the NCAR community atmosphere model (CAM 5.0). NCAR Technical Note
        NCAR/TN-486+ STR 1. 1, pp. 1–12, 2010.

780

        Patera, A. T.: A spectral element method for fluid dynamics: Laminar flow in a channel expansion, J. Comput. Phys., 54, 468–
        488, https://doi.org/10.1016/0021-9991(84)90128-1, 1984.

        The NCAR Command Language (Version 6.6.2) [Software]. Boulder, Colorado: UCAR/NCAR/CISL/TDD.
785   https://doi.org/10.5065/D6WD3XH5, 2019.

        Rayner, N. A., Parker, D. E., Horton, E. B., Folland, C. K., Alexander, L. V., Rowell, D. P., Kent, E. C., and Kaplan, A.:
        Global analyses of sea surface temperature, sea ice, and night marine air temperature since the late nineteenth century, J.
        Geophys. Res. Atmos., 108, https://doi.org/10.1029/2002JD002670, 2003.

790

        Reed, K. A., Jablonowski, C., and Taylor, M. A.: Tropical cyclones in the spectral element configuration of the Community
        Atmosphere Model, Atmos. Sci. Lett., 13, 303–310, https://doi.org/10.1002/asl.399, 2012.

        Reynolds, R. W., Smith, T. M., Liu, C., Chelton, D. B., Casey, K. S., and Schlax, M. G.: Daily high-resolution-blended analyses
795   for sea surface temperature, J. Clim., 20, 5473–5496, https://doi.org/10.1175/2007JCLI1824.1, 2007.

        Rhoades, A. M., Ullrich, P. A., and Zarzycki, C. M.: Projecting 21st century snowpack trends in western USA mountains using
        variable-resolution CESM, Clim. Dyn., 50, 261–288, https://doi.org/10.1007/s00382-017-3606-0, 2018.

800   Roberts, M. J., and Coauthors.: Impact of model resolution on tropical cyclone simulation using the HighResMIP-
        PRIMAVERA multimodel ensemble, J. Clim., 33, 2557–2583, https://doi.org/10.1175/JCLI-D-19-0639.1, 2020.

Sadourny, R.: Conservative finite-difference approximations of the primitive equations on quasi-uniform spherical grids, *Mon. Weather Rev.*, **100(2)**, 136–144, 1972.

805

Taylor, M., Tribbia, J., and Iskandarani, M.: The spectral element method for the shallow water equations on the sphere, J. Comput. Phys., 130, 92–108, https://doi.org/10.1006/jcph.1996.5554, 1997.

Ullrich, P. A.: SQuadGen: Spherical quadrilateral grid generator. University of California, Davis, Climate and Global Change Group software. Retrieved from https://github.com/ClimateGlobalChange/squadgen, 2014.

810 Vitart, F., Anderson, J. L., and Stern, W. F.: Simulation of interannual variability of tropical storm frequency in an ensemble of GCM integrations, J. Clim., 10, 745–760, https://doi.org/10.1175/1520-0442(1997)010<0745:SOIVOT>2.0.CO;2, 1997.

Wang, H., Gao, L., Zhu, L., Zhang, L., and Wu, J.: Changes in the Typhoon Intensity under a Warming Climate: A Numerical Study of Typhoon Mangkhut, J. Clim., 37, 3703–3722, https://doi.org/10.1175/JCLI-D-23-0567.1, 2024.

815

Williamson, D. L., and Co-Authors: The APE Atlas. Technical report, National Center for Atmospheric Research, https://dx.doi.org/10.5065/D6FF3QBR, 2012.

Williamson, D. L.: The effect of time steps and time-scales on parametrization suites, Q. J. R. Meteorol. Soc., 139, 548–560, 820 https://doi.org/10.1002/qj.1992, 2013.

Wu, C., Liu, X., Lin, Z., Rhoades, A. M., Ullrich, P. A., Zarzycki, C. M., Lu, Z., and Rahimi-Esfarjani, S. R.: Exploring a Variable-Resolution Approach for Simulating Regional Climate in the Rocky Mountain Region Using the VR-CESM, J. Geophys. Res. Atmos., 122, 10,939-10,965, https://doi.org/10.1002/2017JD027008, 2017.

825

Wu, G. and Lau, N.-C.: AGCM simulation of the relationship between tropical-storm formation and ENSO, Mon. Weather Rev., 120, 958–977, https://doi.org/10.1175/1520-0493(1992)120<0958:AGSOTR>2.0.CO;2, 1992.

Zarzycki, C. M., Jablonowski, C., and Taylor, M. A.: Using variable-resolution meshes to model tropical cyclones in the 830 community atmosphere model, Mon. Weather Rev., 142, 1221–1239, https://doi.org/10.1175/MWR-D-13-00179.1, 2014.

Zarzycki, C. M. and Jablonowski, C.: A multidecadal simulation of Atlantic tropical cyclones using a variable-resolution global atmospheric general circulation model, J. Adv. Model. Earth Syst., 6, 805–828, https://doi.org/10.1002/2014MS000352, 2014.

835

Zarzycki, C. M. and Jablonowski, C.: Experimental tropical cyclone forecasts using a variable-resolution global model, Mon. Weather Rev., 143, 4012–4037, https://doi.org/10.1175/MWR-D-15-0159.1, 2015.

Zhao, M., Held, I. M., Lin, S. J., and Vecchi, G. A.: Simulations of global hurricane climatology, interannual variability, and

840   response to global warming using a 50-km resolution GCM, J. Clim., 22, 6653–6678, https://doi.org/10.1175/2009JCLI3049.1, 2009.